PPPL-2508

UC-426

PPPL-2508

BROADBAND MEASUREMENTS OF ELECTRON CYCLOTRON EMISSION IN TFTR USING A QUASI-OPTICAL LIGHT COLLECTION SYSTEM AND A POLARIZING MICHELSON INTERFEROMETER

By

F.J. Stauffer, D.A. Boyd, R.C. Cutler, M. Diesso
M.P. McCarthy, J. Montague, R. Rocco

APRIL 1988

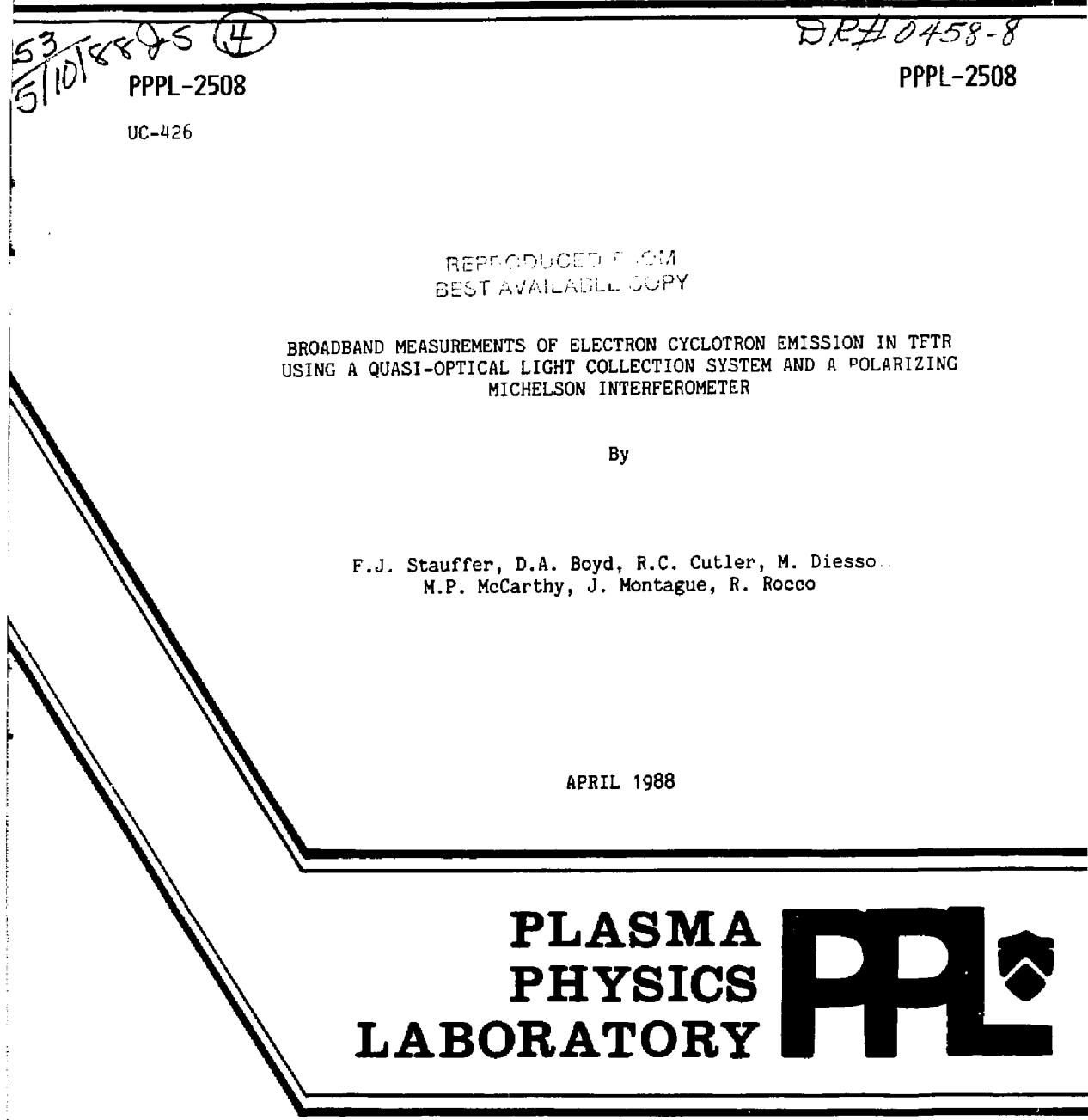

PRINCETON UNIVERSITY
PRINCETON, NEW JERSEY

PREPARED FOR THE U.S. DEPARTMENT OF ENERGY,
UNDER CONTRACT DE-AC02-76-CHO-3073.

NOTICE

Printed in the United States of America

Available from:

National Technical Information Service
U.S. Department of Commerce
5285 Port Royal Road
Springfield, Virginia 22161

Price Printed Copy $__*__; Microfiche $4.50

*Pages	NTIS Selling Price
1-25	$7.00
25-50	$8.50
51-75	$10.00
76-100	$11.50
101-125	$13.00
126-150	$14.50
151-175	$16.00
176-200	$17.50
201-225	$19.00
226-250	$20.50
251-275	$22.00
276-300	$23.50
301-325	$25.00
326-350	$26.50
351-375	$28.00
376-400	$29.50
401-425	$31.00
426-450	$32.50
451-475	$34.00
476-500	$35.50
500-525	$37.00
526-550	$38.50
551-575	$40.00
567-600	$41.50

For documents over 600 pages, add $1.50 for each additional 25-page increment.

PPPL--2508

DE88 009344

Broadband Measurement of Electron Cyclotron Emission in TFTR Using a Quasi-Optical Light Collection System and a Polarizing Michelson Interferometer

F.J. Stauffer and D.A. Boyd

Laboratory for Plasma and Fusion Energy Studies, University of Maryland, College Park, Maryland 20742

R.C. Cutler, M. Diesso, M.P. McCarthy, and J. Montague

Princeton Plasma Physics Laboratory, Princeton, New Jersey 08543

R. Rocco

Ebasco Services Inc., Two World Trade Center, New York, New York 10048

ABSTRACT

For the past three years, a Fourier transform spectrometer diagnostic system, employing a fast-scanning polarizing Michelson interferometer, has been operating on the TFTR tokamak at Princeton Plasma Physics Laboratory. It is used to measure the electron cyclotron emission spectrum over the range 2.5 - 18 cm^{-1} (75 - 540 GHz) with a resolution of 0.123 cm^{-1} (3.7 GHz), at a rate of 72 spectra per second. The quasi-optical system for collecting the light and transporting it through the interferometer to the detector has been designed using the concepts of both Gaussian and geometrical optics in order to produce a system that is efficient over the entire spectral range. The commercial Michelson interferometer was custom-made for this project and is at the state of the art for this type of specialized instrument. Various pre-installation and post-installation tests of the optical system and the interferometer were performed and are reported here. An error propagation

analysis of the absolute calibration process is given. Examples of electron cyclotron emission spectra measured in two polarization directions are given, and electron temperature profiles derived from each of them are compared.

INTRODUCTION

Following the seminal article by Engelmann and Curatolo in 1973,[1] there was a period of rapid development of instruments to exploit the diagnostic potential of electron cyclotron emission (ECE) from tokamaks. G. Tait et al.[2] have summarized the history of this development up to about 1979, when the use of ECE to measure the relative shape of the electron temperature profile had become well established.

There followed a period of a few years during which methods for independently calibrating the instruments absolutely were developed, and advanced systems, such as the Fast-Scanning Michelson Interferometer (FMI) system that is described here, were designed for use on the current generation of large tokamaks. The FMI was placed on TFTR in 1984, and a brief account of the early results was published soon afterward.[3] At that time another ECE diagnostic, a heterodyne radiometer,[4] already was operating, and these two have been used up to the present for making routine measurements of the electron temperature in support of plasma confinement studies on TFTR.[5] Recently, another ECE diagnostic was added, a 20-channel grating polychromator, which is similar to a 10-channel polychromator that was used on the PDX and PLT tokamaks.[6-8]

This paper deals with the design of the FMI system, with special emphasis upon its quasi-optical light collection and transport system. In the years since it was commissioned, numerous performance tests have been carried out on it, and many of these are reported here. The unique advantage of the FMI lies in its broadband spectral range, which always has held out the hope for using the optically thin part of the ECE spectrum to derive the electron density profile. One year after the FMI system was installed on TFTR, a retroreflective viewing target was placed

into the TFTR vacuum vessel in an attempt to control the problem of reflected light that has thwarted that hope up to the present. This paper shows examples of ECE spectra that were measured in two polarization directions before the viewing target was installed. The subsequent effect of the viewing target upon the spectra will be reported in another publication.

I. THE OPTICAL SYSTEM

A. Design Principles

The FMI diagnostic system was designed to measure the first three harmonics of the ECE spectrum in either of two polarization directions. The operating spectral range of 2.5 - 18 cm^{-1} was chosen for measurement over the range of central toroidal magnetic field 3.7-5.2 T.

One of the reasons that the FMI system is comparatively easy to calibrate is that its detector can accept more than one propagation mode from the blackbody calibration source. The total number m of acceptable blackbody modes in one of the two polarization directions is given by:

$$m = A\Omega/\lambda^2 , \qquad (1)$$

where $A\Omega$ is the area-solid angle product (throughput) of the detector and λ is the wavelength.[9] The FMI detector throughput is calculated to be 0.40 cm^2-sr, and so the number of potentially acceptable blackbody modes ranges from 2 at 2.5 cm^{-1} to 129 at 18 cm^{-1}. Therefore, the optical system should be multimoded and matched to the detector. At the same time, a reasonably narrow field of view in the TFTR plasma is required over the entire operating spectral range. Furthermore, the optical system should not scramble the two polarization directions between the point of collection at TFTR and the entrance to the Michelson interferometer, 9.4 m away, where the direction of interest is selected by a polarizer. Finally, the light collection and transport system

must be matched to the detector through the Michelson interferometer, which employs beams propagating in free space. Given these requirements, it was decided to design the FMI optical system to use free space propagation throughout.

Since the FMI operating spectral range includes both the millimeter and submillimeter regions, practical limitations on the size of the imaging components and apertures in the optical system cause it to be quasi-optical, i.e., diffraction is important. In a case such as this, when the light beam is fairly collimated (except at the end, where it enters the detector), the theory of Gaussian beam optics offers a useful design approach for dealing with the diffractive effects at the long wavelength limit.[10] That theory was thoroughly developed during the period 1961-1968 with the aim of applying it to the propagation of microwaves through a confocal lens relay for telecommunications purposes.[11,12] It was found that, in the paraxial limit, radiation propagating through a confocal lens relay can be represented by a linear superposition of normal modes that are called beam modes. These modes are conventionally represented in a cylindrical coordinate system where the z-axis is the optic axis. The radial coordinate r is perpendicular to the z-axis. The radial intensity distribution I(r,z) of the fundamental beam mode has a Gaussian profile that is given by:

$$I = I_0 \exp(-2r^2/w^2), \qquad (2)$$

where w(z) is called the beam radius. The beam is said to form a waist at locations where w has a local minimum.

At its long wavelength limit of 2.5 cm^{-1}, the optical system was designed to transmit just one particular fundamental Gaussian beam mode efficiently (see section I.B); this seems consistent with the above estimate of the available blackbody modes at this end of the range. In particular, we adopted the minimal guideline that every aperture should have a diameter that is at least three times larger than the beam radius of that Gaussian mode at its location. The optical system has to be

consistent with both Gaussian beam optics and geometrical optics in order to make a smooth transition between the two regimes as the spectral frequency increases. As will be seen below, this can be accomplished by confocally spacing all the imaging optics.

B. Light Collection

The front end of the optical system is sketched in Fig. 1. The light-collecting component is a 90 degree off-axis ellipsoidal mirror made of aluminum. Its surface was hand polished to allow aligning the mirror with a He-Ne laser, and then was chromium plated to prevent arc track formation during plasma operations. The mirror is housed inside a standard 4-way cross vacuum component with 10 inch diameter conflat flanges. The collected light is deflected vertically downward to a plane, stainless steel mirror that is housed in a standard "tee" vacuum component with 8 inch diameter conflat flanges. The horizontally deflected light passes from vacuum into air through a wedged, z-cut crystal quartz window with a 10 cm clear aperture.

This periscope arrangement of mirrors was chosen for two reasons. First, it removes the crystal quartz window from a straight line of sight with the plasma, to prevent the buildup of a thin metallic film that can seriously reduce its transmittance. Second, it allows a blackbody source to be placed at the front end of the optics for the purpose of doing an absolute power calibration of the spectrometer over its entire spectral range. For this procedure, the ellipsoidal mirror can be rotated by a vacuum rotary feedthrough, and it can be locked into either of two orientations by using a linear feedthrough to insert a pin into a hole in a metal disk that is attached to the mirror. The locking mechanism was required because the induced eddy current torques on the mirror (its minimum thickness is 2.5 cm) can exceed the torque rating of the rotary feedthrough. The resulting pointing reproducibility of the mirror is approximately 2 milliradians. The calibration source is viewed through a wedged, fused quartz window with a 20 cm clear aperture.

With the exception of passing through the calibration window, the millimeter and submillimeter

emission from the calibration source should couple into the optical system in the same way that ECE from the TFTR plasma does, and a pre-installation test was done to check the equivalence of the two inputs. Figure 2 shows the ratio of the spectrum that was measured with the blackbody calibration source located at the ECE input of the periscope, divided by the spectrum measured with the source at the calibration input (without the window). In spite of the random electronic noise, it is clear that the two inputs are nearly identical. Furthermore, tests have shown that the calibration source fills the field of view.

The transmittance of the calibration window was measured before placing it onto the periscope, and the result is shown in Fig. 3. The solid line shows the measured transmittance, which includes the effects of noise, and the dashed line shows the digitally smoothed curve that is used to compensate for the presence of the window during calibration. The three solid circles show the transmittance that is predicted by a simplified model that assumes an infinite number of incoherent reflections at normal incidence between the two window faces together with absorption on each pass through the average thickness of the window.[13] The material is Spectrosil WF (water-free fused silica) , and it was chosen in an attempt to obtain higher transmittance at the high spectral frequencies than is typical with regular fused quartz, based upon published measurements of its absorption coefficient.[14]

The primary means for controlling the field of view in the TFTR plasma is the field stop aperture that is shown mounted outside the crystal quartz window in Fig. 1. It is located at the short focal point of the ellipsoidal mirror, which has been measured to be 62 cm from the mirror vertex, consistent with its design. In the short wavelength limit of the spectral range, where geometrical optics is pertinent, the mirror focuses a magnified image of the field stop at its long focal point. This point was intended to lie at the position of the viewing target, which is located 291 cm from the mirror vertex (Fig. 4). The actual focal length has been measured to be 310 cm.

The problem of controlling the field of view at the long wavelength limit of the spectral range

led to the choice of the diameter of the ellipsoidal mirror. In microwave theory, the achievement of a fairly collimated antenna pattern leads to the requirement for a minimum size light-collecting aperture whose area is proportional to the axial length of the collimated pattern and the wavelength.[15] These general features appear in a specific way in our optical design approach, which uses Gaussian beam optics for the long wavelength limit of the spectral range. In our case, the analog of a collimated antenna pattern would occur if the waist of the beam mode would lie halfway between the ellipsoidal mirror and the viewing target. The beam radius at the mirror is a function of the beam radius at the waist, and this function can be differentiated to derive the minimum value for the radius at the mirror. The minimum beam radius w at the mirror is given by

$$w = \sqrt{\lambda d/\pi}, \qquad (3)$$

where λ is the wavelength and d is the distance from the mirror to the viewing target. At 2.5 cm^{-1}, w is 6 cm. Thus, a reasonable choice for the mirror working diameter, projected normal to the optic axis, would be 3w, or 18 cm.

Although the model of a Gaussian beam mode with a waist midway between the ellipsoidal mirror and the viewing target guided the choice of the mirror diameter, it was not used for the later stages of the design for two reasons. First, practical considerations forced the use of a somewhat smaller mirror, and it was decided to design on the basis of a 15 cm projected working diameter (5 cm beam radius). Second, and more important, the model included the formation of another waist that was close to, but not at, the location of the short focal point of the mirror, while the scheme for transporting the light to the detector assumes that the waist occurs at the focus. The underlying philosophy of our optical design approach in the long wavelength limit is that, although the ellipsoidal mirror gathers light that can be resolved into a continuum of Gaussian beam modes, only

the particular mode for which the remainder of the optical system has been optimized will be transported efficiently to the detector. In our case, the desired mode at 2.5 cm^{-1} is the one that has a beam radius of 5 cm at the ellipsoidal mirror and a waist at the position of the short focal point. The other modes are expected to diffract out of the system. The choice of this particular mode affects the antenna pattern in both limits of the spectral range in the following ways. At the long wavelength limit, the waist in the vacuum vessel is calculated to occur at a point that is 34%, instead of 50%, of the way from the mirror to the viewing target. The beam radii at this waist and at the viewing target are calculated to be 3.6 cm and 7.8 cm, respectively. At the short wavelength limit, the diameter of the field stop at the location of the short focal point of the ellipsoidal mirror defines the antenna pattern. Since the beam radius of the waist of the mode at this focal point is calculated to be 1.7 cm, the diameter of the field stop was chosen to be 5 cm. Given the ratio of the two measured focal lengths of the ellipsoidal mirror, this leads to a geometrical image of the field stop at the long focal point with a diameter of 25 cm.

C. Light Transport

The radiant energy, focused at the field stop, is coupled through the Michelson interferometer and onto the entrance aperture of the detector enclosure using a series of confocally spaced Gaussian telescopes,[16] consisting of spherical plano-convex TPX lenses and one paraboloidal mirror (Figs. 4 and 5).

Lenses 1 and 2 in Fig. 4 constitute the first of these telescopes. Lens 1 is located with its focal point at the field stop. The distance between lens 1 and lens 2 is equal to the sum of their focal lengths, and the second focal length is longer. The telescope forms a magnified geometrical optics image of the field stop at the location of the focal point of lens 2 that lies in the concrete neutron shield penetration (point A in Fig. 4), and the magnification ratio is equal to the ratio of the two focal lengths. Moreover, it also forms a Gaussian waist at this location with a beam radius that is

larger, by the same magnification ratio, than the radius of the waist at the field stop, and the waist location does not depend upon spectral frequency. These remarkable properties of the Gaussian telescope permitted designing a system that is simultaneously consistent with both Gaussian beam optics and geometrical optics. In particular, the factor of 3 ratio between the field stop diameter and the assumed 2.5 cm^{-1} Gaussian beam radius is preserved everywhere that an image of the field stop is formed. The diameter of each lens (ranging from 12 to 16 cm) was chosen to be at least 3 times larger than the beam radius at its location, and a subsequent geometrical ray tracing analysis indicated that some of the diameters had to be further increased (by up to 12%) to avoid vignetting. Accordingly, the diffractive losses are negligible and the significant transmission losses are due only to reflection and absorption at each lens. Therefore, an iterative procedure was used to find the minimum number of telescopes that could be used to achieve the necessary matching. The result was that three telescopes - one magnifying, a 1:1 relay (forming a field stop image at point B in Fig. 4), and one demagnifying - were used to form a 7 cm diameter image of the field stop at the average location of the scanning mirror (7 cm diameter) of the Michelson interferometer (point C in Fig. 4).

The remainder of the optical system is shown in Fig. 5. The Michelson interferometer configuration is a particular implementation of the Martin-Puplett polarizing interferometer, which is widely used for doing Fourier transform spectroscopy in the millimeter and submillimeter range.[17] The interferometer includes three grids of parallel tungsten wires (10 micron diameter on 25 micron centers). The first of these is used to accept the desired polarization direction into the interferometer while rejecting the unwanted polarization into a dump of microwave-absorbing material (type AN Eccosorb, Emerson & Cuming, Inc.). The second grid splits the light and the resulting two beams are focused by lens 6 onto the two rooftop mirrors. After reflection, the two beams recombine at the beam splitter and pass on to the third wire grid, where the polarization of the beam is filtered again. Regardless of the polarization direction that has been selected by the first

grid, the electric vector of the light leaving the third grid is vertical. The two optical lowpass filters are brass diffraction gratings used in reflection with their rulings perpendicular to the electric vector of the light and parallel to the plane of incidence. The spectral reflectance that was measured for the two filters in tandem is shown in Fig. 6. Values greater than unity for the passband probably resulted from a slight misalignment of the reference mirrors that were installed in place of the gratings for the measurement. When ECE is being measured, the four wire grids labelled as the two stage and single stage attenuators in Fig. 5 are used to reduce the optical transmission by a factor of about 500 in order to keep the detector signal within design limits (see section III. A). For two reasons, the attenuation has been divided between two units. First, our measurements indicate that a high degree of spectrally flat attenuation cannot be provided by only one two-stage attenuator; there is an anomalous leakage at the high end of the frequency range. Second, the attenuation for each unit can be measured more accurately this way. Typical transmission curves for the two units are shown in Fig. 7. The departure from spectral flatness for the single stage attenuator near the rolloff of the optical lowpass filter is not expected on the basis of published measurements of wire grid performance.[18] Perhaps the filter perturbs the polarization state of the light that is incident upon the last wire grid. Lens 7 and the 90 degree off-axis paraboloidal mirror constitute the last Gaussian telescope in the optical system, and they form a geometrical image of the field stop at the input to the compound parabolic concentrator (CPC) with a diameter equal to its aperture.

D. The Detector

The detector is of the InSb hot electron type (QMC Instruments Ltd), and it is kept at liquid helium temperature by means of a cryostat that has a liquid helium capacity of 6 liters and a holdtime of 21 days. The radiation shield of the cryostat is cooled by a liquid nitrogen reservoir with a 4 liter capacity and a 48 hour holdtime.

Optical input to the side-looking cryostat is provided by a room temperature, wedged, TPX

window with a 30 mm clear aperture. The LN-cooled z-cut crystal quartz window in the radiation shield is wedged, with a clear aperture of 16 mm. The clear apertures and spacing of these two windows were chosen to allow the full field of view of the compound parabolic concentrator to be used.[19] Since the input and exit apertures of the 34 mm long concentrator have diameters of 15 mm and 4 mm, respectively, this field of view is calculated to be 31 degrees, and the corresponding throughput is 0.40 cm^2-sr. The exit aperture of the concentrator is the opening to the detector integrating cavity, and the 4 mm diameter of this aperture should allow the efficient collection of light with frequencies down to 1.5 cm^{-1}.[20]

E. Pre-installation Tests

The entire optical system was assembled and tested before it was installed on TFTR. A Gaussian beam simulator[21] was used to test its focusing properties. The simulator uses two revolving off-axis lenses to convert an input He-Ne laser beam into a tube of light. When the light tube is passed through a sequence of imaging components, its diameter changes in the same way that the beam radius of the simulated Gaussian beam mode would do. The simulator was used to align the components and to set their separations, which were found to agree with the specified focal lengths to within 6%. It confirmed that the imaging of a 2.5 cm^{-1} Gaussian beam mode from the field stop to the compound parabolic concentrator input would occur as planned.

A long wavelength antenna pattern test also was done. A modulated 70 GHz (2.3 cm^{-1}) Gunn oscillator fed energy into an untuned cavity fitted with a mode scrambling device,[22] and the microwaves were output through a compound parabolic concentrator antenna with a 15 mm diameter aperture. The antenna was placed at a location corresponding to the position of the viewing target. This should have created a nearly planar wavefront at the mirror. The gathered light passed through the entire optical system including the Michelson interferometer (with one mirror blocked to avoid interference effects) and the detector signal was fed to a lock-in amplifier.

The antenna was moved transverse to the optic axis, and the resulting detected intensity profile agreed well with a Gaussian shape, but the beam radius was 13% larger than expected on the basis of the assumption of a waist located at the field stop with a beam radius one-third the diameter of the stop. Nevertheless, this result generated confidence in our long wavelength optical design approach.

An effort was made to measure the efficiency of the optical system. The spectrum of the blackbody was measured when it was placed in its normal position at the calibration input to the periscope, and this was compared to the spectrum measured when it was placed directly in front of lens 6, which is mounted at the input to the Michelson interferometer. Neither of the quartz windows was mounted on the periscope for this test, so the losses should have been due entirely to the five lenses between those two locations. The reflection loss per lens is estimated to be 0.31 dB, independent of frequency. The absorption loss per lens (with average thickness of 1 cm) increases with frequency due to the use of TPX. The total predicted loss ranged from 1.9 dB at 4 cm^{-1} to 4.7 dB at 20 cm^{-1}. The measured loss at these two frequencies was 5.7 dB and 7.2 dB. The reason for this frequency-dependent discrepancy is not understood.

II. THE MICHELSON INTERFEROMETER

There were three main objectives in the design of the Fast-Scanning Michelson Interferometer, which was custom-made (Specac, U.K.) for the TFTR project. First, it was to have a spectral resolution that was about the same as had been achieved with Fabry-Perot interferometers and grating polychromators that were being used to measure ECE from tokamaks. Second, it was to scan repetitively with a period that was about the same as had been achieved with the lower resolution Michelson interferometers that were being used to measure ECE from tokamaks. Finally, its optical throughput was to be large enough to take full advantage of the detector

throughput in order to minimize the time required to calibrate. The resulting instrument offers a combination of spectral resolution and repetition rate that is at the state of the art for this type of spectrometer.

Plan and elevation views of the FMI are shown in Fig. 8. The 1 HP induction motor is linked to the rotary crank (designed for a motorcycle engine) by a matched pair of vee belts. The rotary crank drives the square, flat air bearing at a reciprocation frequency of 36 Hz. A rod-end coupling connects this bearing to the shaft air bearing, which carries the scanning mirror. The length of the stroke is 4.95 cm. The locations of the two photoelectric sensors near the turnaround points mark the endpoints of the 4.65 cm long portion of the stroke that is used to collect data, which is called the "active scan." It was decided to stop taking data when the mirror velocity falls below one-third of its maximum velocity. The duration of the active scan is 11 ms. Data collection occurs during the active scan in each of the two directions (forward and reverse) so that two interferograms are measured for each reciprocation cycle. The displacement of the fiducial mark on the mirror shaft as it travels between the two sensors is measured by a Moire fringe system that utilizes a grating of reflective stripes that is attached to the shaft. By dividing down the signal due to the basic 40 micron physical spacing of the stripes, a selection of interferogram sample intervals is made available. On this instrument, the interferogram can be sampled in physical path increments of 40, 80, 120, and 160 microns. The smallest sample interval sets the maximum measurable spectral frequency at 62.5 cm^{-1} (1874 GHz), while the larger intervals are provided for economy of data storage, since a more restricted spectral range is adequate for ECE measurements on TFTR. The instrument provides two digital logic (TTL level) signals that are called STATUS and CLOCK. STATUS is used to organize data acquisition into units of a forward-reverse pair of interferograms. CLOCK is a square wave that is generated by the Moire fringe system, and it is used to digitize each interferogram in equal increments of scanning mirror displacement. Since the velocity of the scanning mirror varies by a factor of 3 during each active scan, the frequency of CLOCK varies

accordingly. The maximum sampling frequency is given by the product of the maximum optical sampling rate (125 cm^{-1}) multiplied times the maximum rate at which the scanning mirror sweeps out the optical path (1111 cm/s), and it is equal to 139 kHz.

In order to position and align the stationary mirror, an adjustable mount has been provided that allows movement in all six degrees of freedom (rotational and translational). The stationary mirror is positioned so that the grand maximum of the interferogram lies 0.1 of the way between the two endpoints of the active scan for the purpose of phase correction (see section III. C.). Then, the maximum available optical path difference associated with the longer, right-hand side of the interferogram is 8.37 cm, which yields a spectral resolution (see section III. C.) of 0.10 cm^{-1} (3 GHz), and the maximum resolving power of the instrument is 625.

The diameters of the two mirrors of the Michelson interferometer were chosen to conserve the available throughput of the detector without degrading the maximum spectral resolving power . The limiting resolving power is inversely proportional to the solid angle Ω that corresponds to the divergence of the light beam falling on the mirrors.[23] Therefore, the maximum resolving power of 625 leads to an upper bound on Ω, which in turn leads to a lower bound on the mirror area A. In this way, the diameter of the mirrors was chosen to be 7.0 cm. It is important to note that the tolerance on the pointing direction of the scanning mirror becomes smaller as both the mirror diameter and the spectral frequency increase. The peak to peak "wobble" of the scanning mirror as it moves is 0.5 arc minute, which is good enough to ensure at least 95% interferometric modulation, even at the highest measurable spectral frequency of 62.5 cm^{-1}. [24]

III. DATA PROCESSING

A. Signal Conditioning

As shown in Fig. 9, mercury batteries and a metal film load resistor are used to produce a low

noise circuit that passes a bias current of 39 microamps through the InSb detector. If the radiant energy that is concentrated on the detector increases, its electrical resistance decreases. For sufficiently small changes, the resulting decrease of the voltage difference across the detector is linearly proportional to the change in the integral of the radiant power spectrum, weighted by the spectral response of the detector. Tests with a microwave source have shown that the detector remains linear for voltage changes of up to at least 68 mV from its background radiation bias point of 470 mV, but wire grid attenuators are used to keep the AC signal less than 10 mV, which is the maximum input range of the preamplifier (see section I.C).

The maximum detector signal frequency that can result from the modulating action of the Michelson interferometer is the product of the maximum measurable spectral frequency (62.5 cm^{-1}) multiplied times the maximum rate at which the scanning mirror sweeps out the optical path (1111 cm/s). It equals 69.4 kHz, which is well within the signal bandwidth of the InSb detector.

As shown in Fig. 9, the detector is AC coupled to a low noise preamplifier (Brookdeal 5004). Only its first stage (gain 60) is used so that it can be followed by a programmable postamplifier in order to obtain enough flexibility in the remote-controlled net gain of the circuit. Typically, the signal is amplified to several volts before it is transmitted to the digitizer. The two amplifiers are powered from a rechargeable battery pack in an effort to minimize noise.

As shown in Fig. 10, the custom-made Gating, Counting & Timing Unit (GCTU) is a multipurpose interface between the analog and digital signals that are output by the postamplifier and the FMI, respectively, and the digitizers. The incoming analog (interferogram) signal is passed through an active electronic lowpass filter that is intended to prevent the aliasing of high frequency noise into the measured spectrum. This filter poses a potential problem because its associated time delay destroys the synchronization between the analog signal and the CLOCK sampling signal. Since the scanning mirror velocity varies during the active scan, this might lead to spectrum errors known as ghosts. The three-part solution, for a system like ours, that is given in the literature is:

(1) use a Bessel filter, (2) introduce a delay into the digital signal to compensate for the filter delay, and (3) set the filter edge to be at least twice the highest signal frequency in the interferogram.[25] The last point implies significant oversampling of the interferogram in order to ensure that there is no noise aliasing, and this carries the penalty of increased data storage and FFT computation time. Obviously, the first step in minimizing this penalty is to limit the highest spectral frequency to the lowest acceptable value. In our case, the optical lowpass spectral filter with its edge at 18.6 cm^{-1} limits the highest interferogram signal frequency to 20.7 kHz. We have compromised on the guideline by using a 4-pole Bessel filter with an edge at 29.8 kHz. Furthermore, in order to hold down the data handling requirements, we have chosen an 80 micron physical sample interval (62.5 cm^{-1} sampling rate), which is more than adequate for sampling the interferogram, but its associated clock frequency range of 23 - 69 kHz does allow the possibility of noise aliasing when the mirror velocity falls below 86% of its maximum value. Nevertheless, when a measurement of the calibration source spectrum was done at this sampling rate, no perceptible degradation in the signal to noise ratio was found, relative to the same measurement done at twice the sampling rate. A shift register was designed into the GCTU to introduce a time delay into the STATUS and CLOCK signals to compensate for the cumulative delay in the analog circuit, but the delay is less than one-half of the minimum CLOCK period. In order to test its effect, the spectrum of an 83 GHz microwave source was measured with the delay in or out, and no difference could be seen. Nevertheless, the delay is used routinely.

B. *Data Acquisition*

The data acquisition process depends upon whether calibration or ECE measurement is being done. For calibration, thousands of forward-reverse pairs of interferograms from a blackbody source are averaged to enhance the signal-to-noise ratio. As shown in Fig. 10, the conditioned analog and digital signals pass directly from the GCTU to a signal averager (Nicolet 12/70),

which has an 8-bit, 500 kHz ADC and a 20-bit memory word. The ADC resolution is more than sufficient, given the signal-to-noise ratio of the calibration source interferogram.[26] The summed data are then transferred to the data analysis computer via a CAMAC graphics buffer module that serves as an RS-232C interface. Including user interaction time, the transfer requires approximately 30 seconds.

For ECE measurement, interferogram pairs from the plasma are directed to two 12-bit, 200 kHz transient digitizer CAMAC modules, each addressing 128K of buffer memory, in order to measure the time evolution of the ECE spectrum during a plasma discharge. For this purpose, the GCTU performs four vital functions. First, it switches the signal from one digitizer to the other when the first 128K block of buffer memory is nearly full. Second, it gates the digital signals on, only during the time periods when acquisition of interferograms is desired. This feature is programmable so that plasma discharges lasting longer than 6.3 seconds, which is the buffer memory limit for continuous acquisition, can be accommodated by gating off acquisition during less interesting parts of the discharge. Of course, gating is done so that complete STATUS cycle units are always collected. Third, the number of CLOCK pulses in each acquired STATUS cycle is counted (this number should always be the same) and stored in a CAMAC module for use in separating the contiguously stored interferogram pairs during data analysis. Fourth, the time of occurrence of the end of each acquired STATUS cycle is measured and stored in another CAMAC module in order to assign a time to each acquired interferogram.

C. *Data Analysis*

The interferogram data that are stored in the CAMAC buffer memory are archived on the computer after each plasma discharge, and all data analysis is carried out there. Given the 4.65 cm long active scan and sampling rate of 62.5 cm^{-1}, an interferogram contains 581 data points, but the fast Fourier transform package (FFT) requires a binary multiple of points. In order to save

computation time, which is important for analysis between plasma discharges, as well as data storage space, the interferogram is truncated to 512 points, which results in a tolerable degradation of the spectral resolution. Consistent with standard practice in Fourier spectroscopy, the interferogram is multiplied by a weighting function (apodization function) before it is submitted to the FFT, and this function can be set to zero in order to implement the truncation. Figure 11 shows a typical, truncated, ECE interferogram and two weighting functions that follow the recommendations of Mertz.[27] The position of the stationary mirror of the Michelson interferometer has been set so that the portion of the waveform that is symmetric about the grand maximum will yield adequate spectral resolution of the broad features of the spectrum for the purpose of phase correction.[28] The symmetric triangular weighting function shown by the short dashed lines is applied to this smaller interferogram for that purpose. The left side of the asymmetric triangular weighting function shown by the long dashed lines ensures that the features around the grand maximum are not double-weighted when the FFT of the larger interferogram is computed, and the right side serves to reduce the sidelobes in the instrument line shape . The line shape that results from the asymmetric triangular weighting function was measured by processing the interferogram from an 83.3 GHz (2.78 cm^{-1}) microwave source, and it is shown in Fig. 12. The interferogram was truncated to 512 points and then zeroes were appended to it to form an interferogram four times larger in order to produce an interpolated spectrum that would reveal the line shape better. Theory predicts that the FWHM (in units of cm^{-1}) of the line shape should be given by

$$FWHM = 0.875/D, \tag{4}$$

where D is the maximum optical path difference in the interferogram. In this case, the expected FWHM is 0.121 cm^{-1}, which agrees well with the measured value of 0.123 cm^{-1} (3.7 GHz).

The FFT that is used to produce spectra is a FORTRAN implementation of an algorithm by

Bergland.[29] It is specialized for computing the FFT of a real interferogram, and it takes advantage of the fact that the transform is Hermitean by computing only the non-redundant components of the real and imaginary parts of the spectrum. Each 512-point interferogram is Fourier transformed to produce a 256-point spectrum, and the complete process of apodizing and transforming the symmetric and asymmetric portions of one interferogram and carrying out the phase correction requires 39 ms of CPU time on the Gould 32/87 data analysis computer.

IV. MEASUREMENT OF ECE SPECTRA

A. Absolute Calibration

The calibrated, measured ECE spectrum is derived by dividing the Fourier transform of the ECE interferogram by the spectrally independent value of the net transmission of the wire grid attenuators, the amplifier gain, and the instrument response spectrum. This section describes the procedure for measuring the latter and offers an estimate of the random error in the calibrated ECE spectrum.

The instrument response spectrum can be determined by measuring an interferogram from a calibration source with a known spectrum. As shown in Fig. 1, our choice is a mass of microwave absorber (type CV Eccosorb), which is a good approximation to a blackbody in the millimeter and submillimeter region. Since its effective temperature (see below) is five orders of magnitude smaller than the temperature of the plasma electrons in TFTR, the wire grid attenuators are set for 100% transmission, and the interferogram signal must be averaged (see Section III.B). In order to eliminate contributions to the signal that are not due to the calibration source, interferograms are averaged with the absorber at room temperature and at liquid nitrogen temperature, and their difference, divided by the amplifier gain, is Fourier transformed to produce a source spectrum such as the one shown by the dashed line in Fig. 13. It represents the difference between 36,000 scans

at room temperature and 31,600 scans at liquid nitrogen temperature. Then, the instrument response spectrum (solid line in Fig. 13) is derived in two steps. First, the source spectrum is divided by the difference of two Planck functions, evaluated at the two temperatures. Second, the resulting spectrum is divided by the calibration window transmittance spectrum that is shown by the dashed line in Fig. 3.

Instrument response spectra are measured and used for each of the two directions of travel of the scanning mirror because the interferogram grand maximum location typically differs by one sample point in the two cases. The ratio of the spectra is unity to within about 2%. Furthermore, response spectra are measured and used for each of the two polarization directions, and here the difference is larger. In the case for which the electric vector of the light is vertical as it leaves the tokamak, the vector lies in the plane of incidence for the four mirrors that it encounters before entering the Michelson. According to theory,[30] the mirror reflectance should be lower for this direction than for the horizontal direction, and the response spectra for the vertical direction are found to be systematically lower than those for the horizontal direction by about 5%.

The reproducibility of the instrument response spectrum is illustrated by Fig. 14, which shows the ratio of the response spectrum from Fig. 13 divided by another response spectrum that was measured with the same optical configuration three weeks later. The larger deviations below 5 cm^{-1} in Fig. 14 probably reflect the poorer signal-to-noise ratio due to the decrease of the intensity of the calibration source at lower frequencies. The two water vapor absorption line features at 12.7 and 14.9 cm^{-1} resulted from the higher relative humidity for the earlier measurement (45% compared to 35%). In the region of the response spectrum from 5 to 12 cm^{-1}, which is typically used to derive the electron temperature profile from the second harmonic ECE feature for TFTR (see the following section), the variation due to random noise in the detector circuit is about 2%.

An estimate of the random error in the calibrated ECE spectrum involves the combination of the estimated random errors for seven factors: the detector circuit electronic noise for the measurement

of both the blackbody source and the ECE, errors in measuring the amplifier gain in each of the two cases, errors in the measurement of the total attenuation factor and the transmission of the calibration source viewing window, and the error in the positioning of the detector cryostat. Based upon the discussion of Fig. 14 above, the random error in the measurement of the blackbody source spectrum due to detector circuit noise is estimated to be 2%. An indication of the signal-to-noise ratio during ECE observations was obtained by using a shutter to block the ECE from the detector and then carrying out the procedure to derive electron temperature from the measured signal. The noise in the detector circuit corresponded to an electron temperature of 10 eV, and this can be interpreted roughly as a 1% random error due to electronic noise. The uncertainty in the measurement of the amplifier gain in each case is about 2%. The uncertainties in the measurement of the total attenuation and the window transmission (see solid line in Fig. 3) are estimated to be 2% and 3%, respectively. Finally, it should be mentioned that the detector cryostat sometimes is moved for the purpose of transferring liquid helium, but a test has shown that its location is reproduced accurately enough so that the associated variation in the response curve level is only about 1%. When all of the above random errors are added in quadrature, they yield a total random error estimate of 5% for the calibrated ECE spectrum, and hence for the electron temperature measurement.

B. Comparison of the Two Polarization Directions

The optical system has been designed to allow the measurement of the ECE spectrum in either of two orthogonal polarization directions, i.e., with the electric vector either vertical or horizontal as the light leaves the tokamak. In this paper, these directions are called V-Mode and H-Mode, respectively. Since the input wire grid of the Michelson interferometer is used to select the polarization direction that will be observed, there should be negligible polarization scrambling by the optical system up to that point. In order to test this, a wire grid, oriented to pass the H-Mode

through to the ellipsoidal mirror, was placed between the calibration source and the calibration window (see Fig. 1). The ratio of the spectrum that was measured with the Michelson input grid oriented for V-Mode, divided by the spectrum measured with it oriented for H-Mode, is shown in Fig. 15. Thus, the cross-polarization associated with the optics in front of the Michelson is at the level of 1 to 2%, and virtually the same result was obtained when the grid in front of the calibration window was turned to the V-Mode.

Due to the helical magnetic field lines at the plasma edge, the V-Mode consists almost entirely of extraordinary mode emission, with a small admixture (typically 2% for TFTR) of ordinary mode, and vice-versa for the H-Mode. The use of the optically thick portions of the spectrum in either of these two polarization directions to derive the plasma electron temperature profile is now a commonplace on most tokamaks.[31] While the potential for using the optically thin portions in either of the two polarization directions to derive the plasma electron density profile in a tokamak has long been recognized,[1] attempts to realize it in practice have been thwarted by the effects of the reflective vacuum vessel. Beginning with the first reported measurements of ECE spectra in a tokamak,[32] researchers have tried to understand the observed level of the optically thin emission by assuming a model of infinitely many reflections that can enhance it through multiple passes through the plasma and that can couple energy from one polarization direction into the other.

The effects of the TFTR vacuum vessel upon the ECE spectrum can be seen in Fig. 16, which shows V-Mode and H-Mode spectra that were measured for two essentially identical TFTR discharges before the viewing target was installed. The optically thin portions of the spectra can be analyzed using a model for an infinite number of multiple reflections that has appeared in the literature.[33] There, it is hypothesized that the total reflectivity of the vacuum vessel wall consists of the sum of two parameters q and p, where q is the fraction of incident light that is reflected into the same polarization direction, and p is the fraction that is reflected into the orthogonal direction. The spectra in Fig. 16 yield the values q = 44% and p = 24%. The temperature profiles that were

derived from the optically thick portions of the spectra are shown in Fig. 17. Only a part of the temperature profile can be measured using the V-Mode second harmonic feature due to overlap with the third harmonic feature. The profiles are not corrected for the effects of the plasma current and the plasma diamagnetism upon the vacuum magnetic field,[34] but this is not needed for the comparison that is being made.

One year after the TFTR FMI system began operating, a retro- reflecting target was installed as part of the toroidal limiter on the back wall of the vacuum vessel (see Fig. 4). It was designed to control the reflections in such a way as to permit electron density profiles to be measured. The results of that experiment will be reported in another publication.

ACKNOWLEDGMENTS

The success of this diagnostic system has resulted from the good work of many competent people at Princeton Plasma Physics Laboratory, the University of Maryland, and elsewhere. Among those at PPPL, special thanks are due to: K.M. Young and L.C. Johnson for their support, advice, and encouragement; V. Corso and T. Provost for advice and assistance with the vacuum preparation of the periscope; M.A. Goldman and J. Doane for advice about quasi-optics and assistance with microwave measurements; D.L. Collins for establishing the technical feasibility of using a motorcycle engine crank to drive an air bearing that would carry the Michelson scanning mirror; G. Tait for designing the low-pass spectral filter and for many enlightening discussions, especially about calibration; J. Gulizio for engineering the electrical system; V. Gambino and B. Phillips for their assistance in purchasing critical items; and A. Cavallo, P.C. Efthimion, and G. Taylor for helpful suggestions. Among those at the University of Maryland, J. Fischer and J. Benson provided spectroscopic measurements that aided the optical design, and A. Murdoch and S. Guharay made important contributions by using a Gaussian beam simulator to characterize the ellipsoidal mirror and to test and align the optics. B. Hawker and his staff at Specac played a crucial role by producing the Michelson interferometer. H. Watson and his staff at Culham Laboratory performed a valuable service by using their aluminum diffusion bond process to vacuum seal the crystal quartz window that is used to view the ECE. This work was supported by U.S. DoE contract No. DE-AC02-76-CH0-3073 .

REFERENCES

1 F. Engelmann and M. Curatolo, Nucl. Fusion 13, 497 (1973).

2 G.D. Tait, F.J. Stauffer, and D.A. Boyd, Phys. Fluids 24, 719 (1981).

3 F.J. Stauffer, D.A. Boyd, R.C. Cutler, and M.P. McCarthy, Rev. Sci. Instrum. 56, 925 (1985).

4 G. Taylor, P.C. Efthimion, M.P. McCarthy, E. Fredd, M.A. Goldman, and D. Kaufman, Rev. Sci. Instrum. 56, 928 (1985).

5 F.J. Stauffer, P.C. Efthimion, G. Taylor, V. Arunasalam, D.A. Boyd, R.C. Cutler, M.P. McCarthy, D.A. Rasmussen, and J. Wilgen, in Proceedings of the Fifth International Workshop on Electron Cyclotron Emission and Electron Cyclotron Heating, edited by R. Prater and J. Lohr (General Atomic, San Diego, 1985) p. 18.

6 J. Fischer, D. Boyd, A. Cavallo, and J. Benson, Rev. Sci. Instrum. 54, 1085 (1983).

7 A. Cavallo, H. Hsuan, D. Boyd, B. Grek, D. Johnson, A. Kritz, D. Mikkelsen, B. LeBlanc, and H. Takahashi, Nucl. Fusion 25, 335 (1985).

8 A. Cavallo and R. Cutler, Rev. Sci. Instrum. 56, 931 (1985).

9 H. Kogelnik and A. Yariv, Proc. of IEEE 52, 1 (1964).

10 D.H. Martin and J. Lesurf, Infrared Phys. 18, 405 (1978).

11 G. Goubau, *Advances in Microwaves*, (Academic Press, New York, 1968), Vol 3, p. 67.

12 D. Marcuse, *Light Transmission Optics*, 2nd Ed., (Van Nostrand Reinhold Co., New York, 1982), Chap. 5.

13 G.W. Chantry, *Submillimetre Spectroscopy* (Academic, New York, 1971), p. 65.

14 M.N. Afsar and K.J. Button, IEEE Trans. Microwave Theory Tech. MTT-31, 217 (1983).

15 J.F. Ramsay, *Advances in Microwaves* , edited by L. Young (Academic, New York, 1968), Vol. 3, p. 128 .

16 P.F. Goldsmith, *Infrared and Millimeter Waves* , edited by K.J. Button (Academic, New York, 1982), Vol. 6, p. 277.

17 D.H. Martin, *Infrared and Millimeter Waves* , edited by K.J. Button (Academic, New York, 1982), Vol. 6, p. 66.

18 J.A. Beunen, A.E. Costley, G.F. Neill, C.L. Mok, T.J. Parker, and G. Tait, J. Opt. Soc. Am. 71, 184 (1981).

19 W.T. Welford and R. Winston, *The Optics of Nonimaging Concentrators* (Academic, New York, 1978), p. 48.

20 D.A. Harper, R.H. Hildebrand, R. Stiening, and R. Winston, Appl. Opt. 15, 53 (1976).

21 J.A. Arnaud, Am. J. Phys. 41, 549 (1973).

22 H.A. Gebbie and D.T. Llewellyn-Jones, Int. J. Infrared Millimeter Waves 2, 197 (1981).

23 R.J. Bell, *Introductory Fourier Transform Spectroscopy* (Academic, New York, 1972), p.149.

24 J. Chamberlain, *The Principles of Interferometric Spectroscopy* (Wiley, New York, 1979) pp. 237-238.

25 A.S. Zachor and S.M. Aaronson, Appl. Opt. 18, 68 (1979).

26 J.W. Cooper, Computers and Chem. 1, 55 (1976).

27 L. Mertz, Infrared Phys. 7, 17 (1967).

28 C.D. Porter and D.B. Tanner, Int. J. Infrared Millimeter Waves 4, 273 (1983) .

29 G.D. Bergland, Commun. ACM. 11, 703 (1968).

30 F.A. Jenkins and H.E. White, *Fundamentals of Optics*, 3rd ed. (McGraw-Hill, New York, 1957), p. 521.

31 F.J. Stauffer, *Temperature, Its Measurement and Control in Science and Industry*, edited by J.F. Schooley (American Institute of Physics, New York, 1982), Vol. 5, p. 687 .

32 A.E. Costley, R.J. Hastie, J.W.M. Paul, and J. Chamberlain, Phys. Rev. Lett. 33, 758 (1974).

33 I.H. Hutchinson and D.S. Komm, Nucl. Fusion 17, 1077 (1977).

34 W.H.M. Clark, Plasma Physics 25, 1501 (1983).

FIGURE CAPTIONS

Fig. 1 The front end of the optical system, shown with the calibration source in place.

Fig. 2 The ratio of the calibration source spectrum viewed through the vacuum vessel side of the periscope, divided by the spectrum viewed through the calibration side (without the window).

Fig. 3 Measured (solid line) and smoothed (dashed line) spectral transmittance of the calibration window. For comparison, the solid dots show three values calculated from a simplified model.

Fig. 4 Elevation view of the optical system up to the Michelson.

Fig. 5 Plan view of the Michelson/Detector interface optics.

Fig. 6 Measured reflectance of the two low-pass filters.

Fig. 7 Examples of the transmittance of the single and two stage wire grid attenuators.

Fig. 8 Plan and elevation views of the Fast-Scanning Michelson Interferometer.

Fig. 9 The circuit for biasing the detector and amplifying the signal.

Fig. 10 Block diagram for the data acquisition electronics.

Fig. 11 Typical ECE interferogram, showing its apodization function (long dashes). The other weighting function (short dashes) is applied to the symmetric part of the interferogram for the purpose of phase correction.

Fig. 12 The measured instrument line shape that results from the apodization function that is shown by long dashes in Fig. 11.

Fig. 13 The measured spectrum of the calibration source (dashed line) and the instrument response spectrum (solid line) that is derived from it. Note the two prominent water vapor absorption lines.

Fig. 14 The ratio of the instrument response spectrum from Fig. 13, divided by another response spectrum that was measured three weeks later. The two water vapor absorption lines show that the climate was more humid for the earlier measurement.

Fig. 15 The measured cross-polarization ratio for the optical system in front of the Michelson.

Fig. 16 Comparison of the V-Mode and H-Mode ECE spectra, for two essentially identical TFTR discharges, before the viewing target was installed. The first four ECE harmonic features have been numbered.

Fig. 17 Electron temperature profiles derived from the two spectra in Fig. 16.

#87X0286

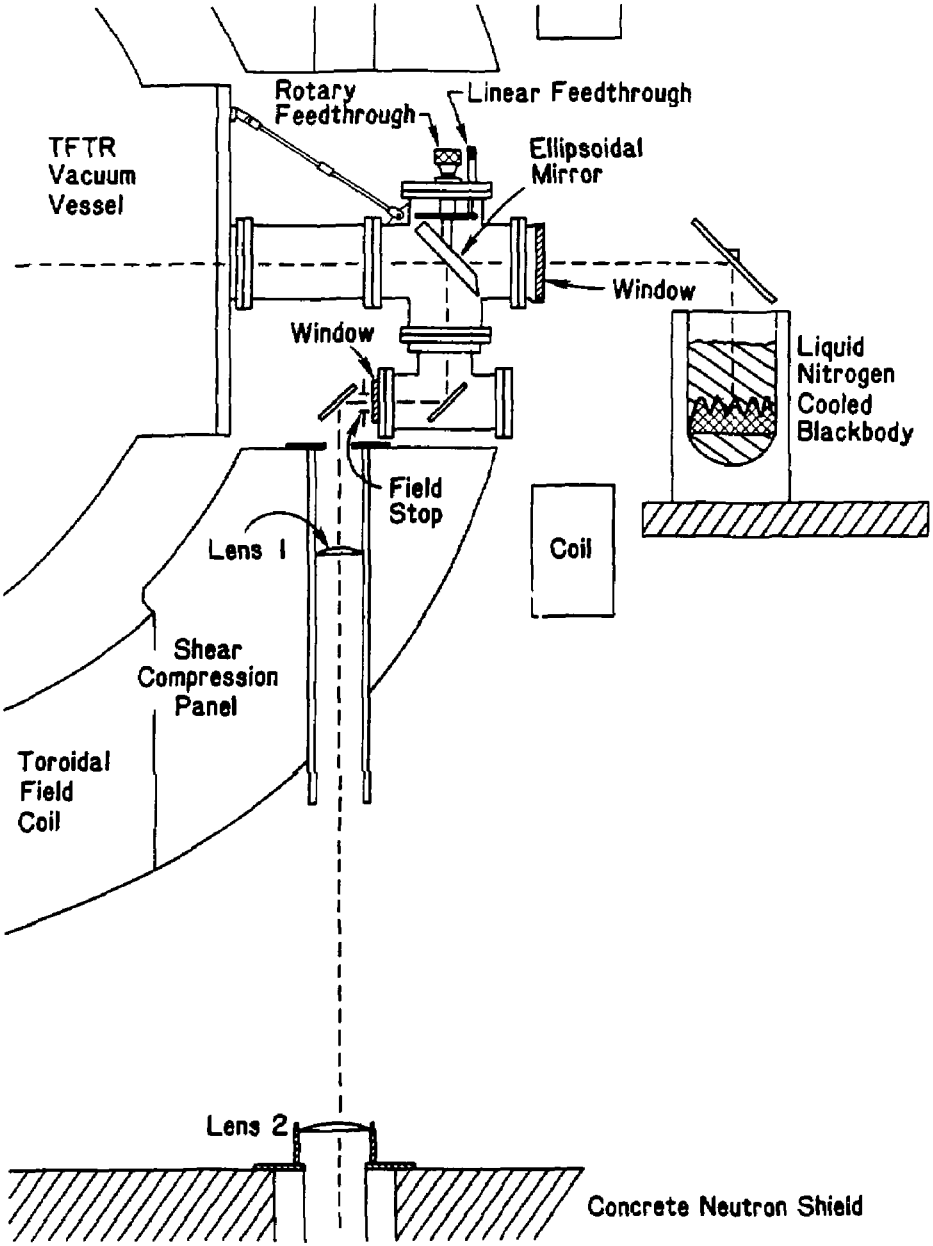

Fig. 1

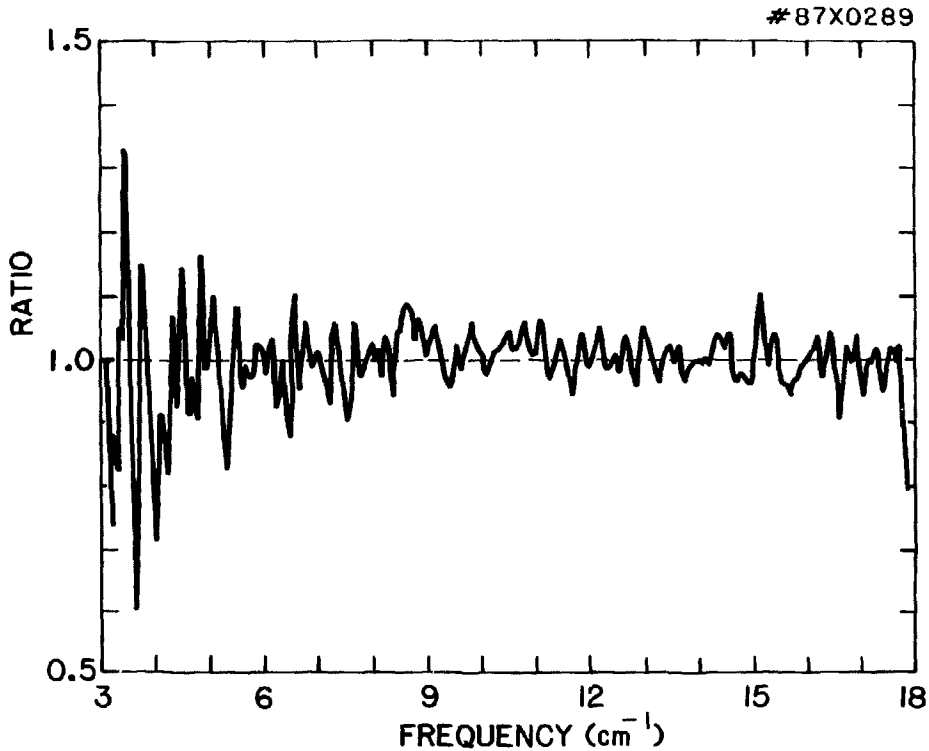

Fig. 2

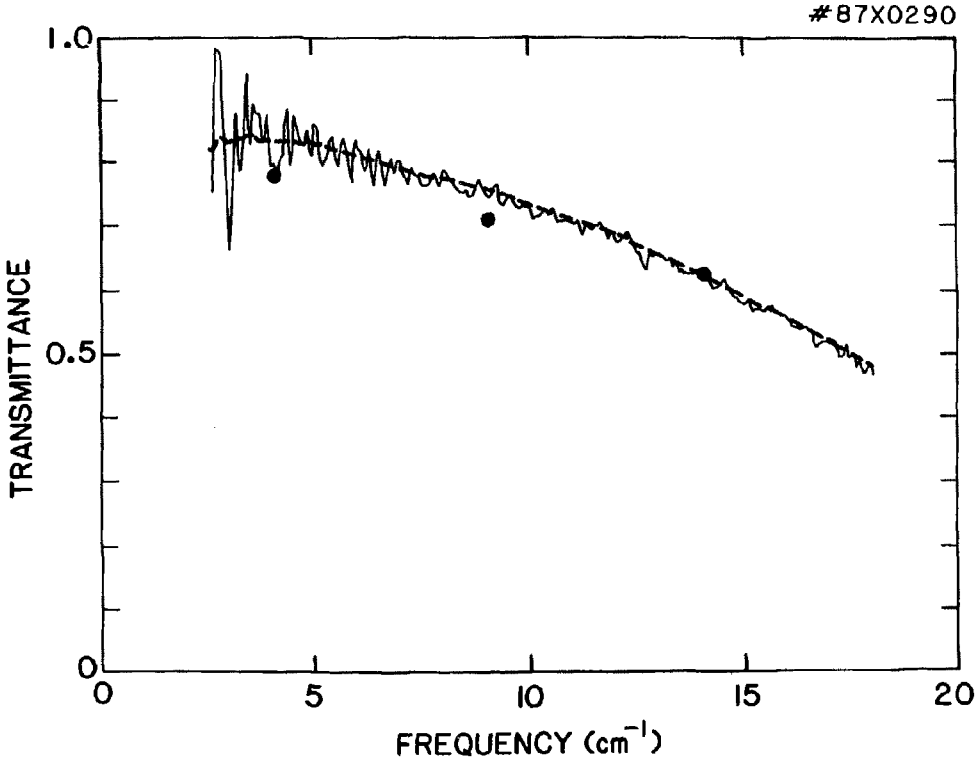

Fig. 3

#87X0306

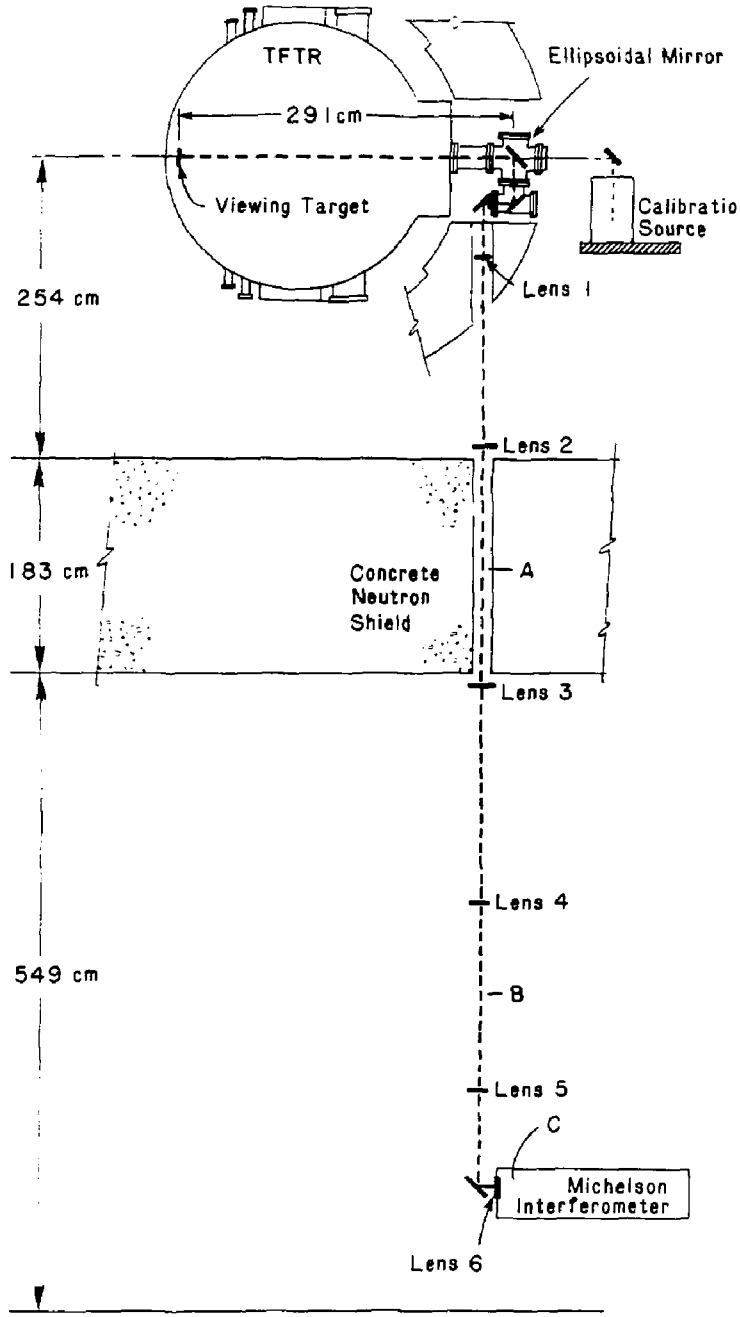

Fig. 4

#87X0285

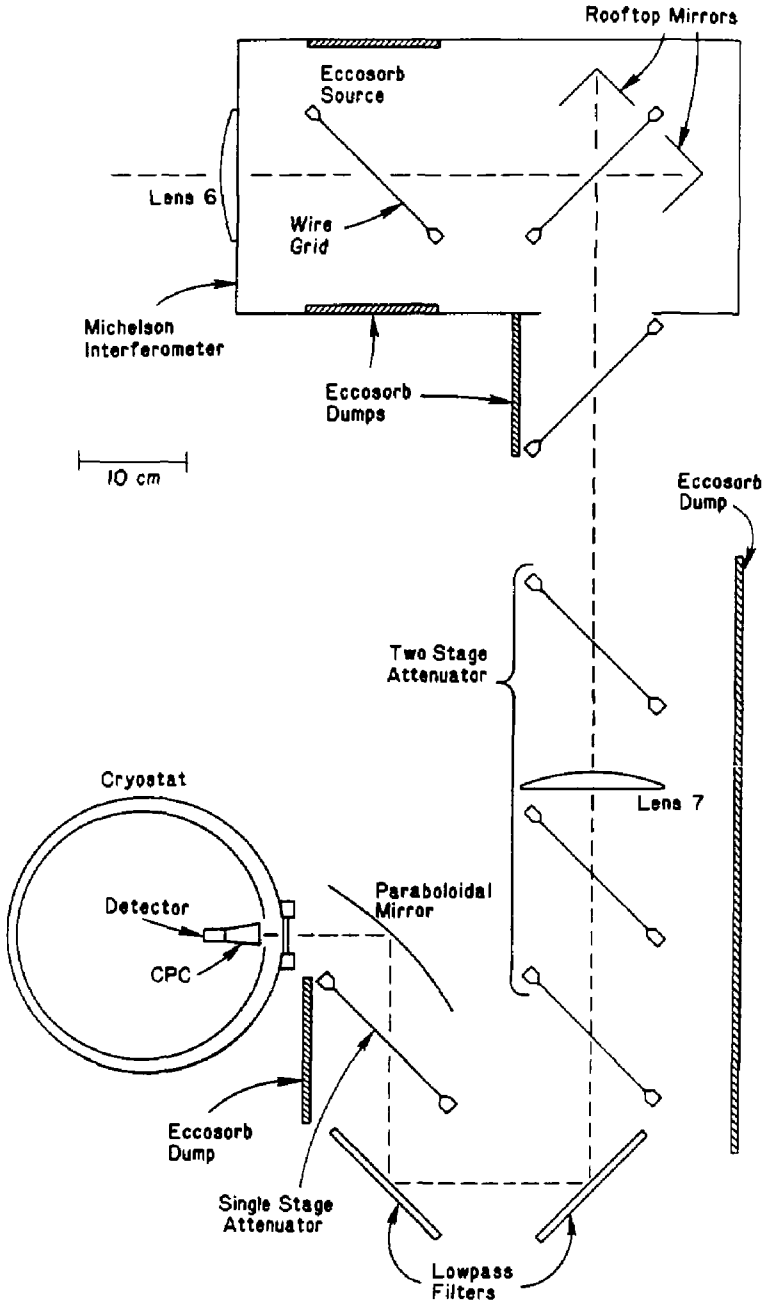

Fig. 5

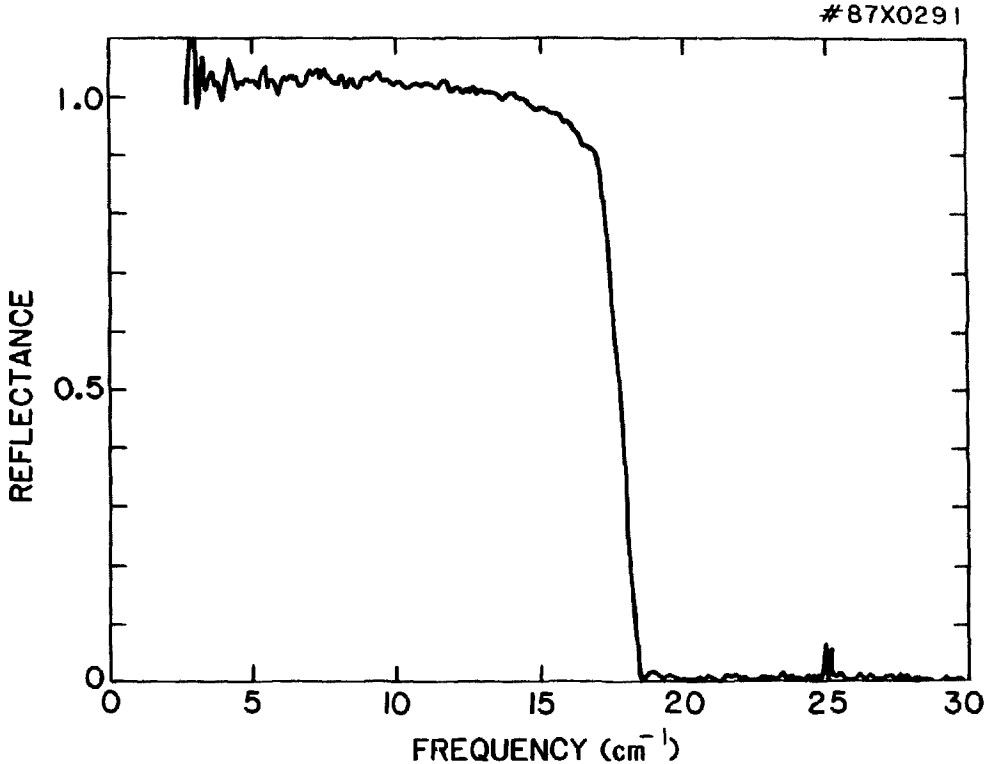

Fig. 6

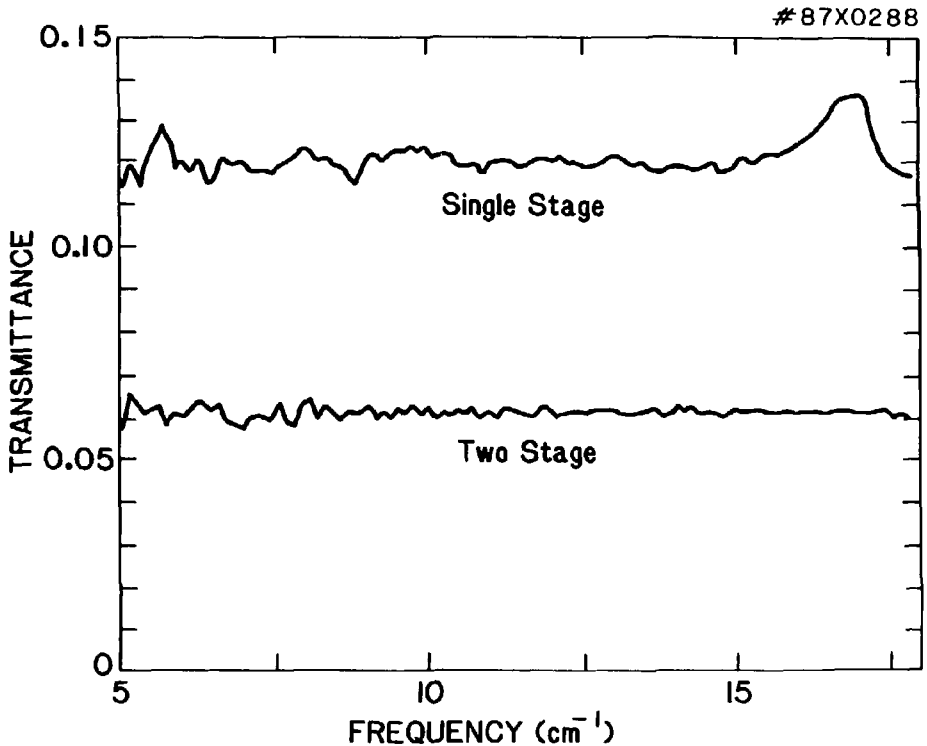
#87X0288
0.15
0.10
0.05
0
TRANSMITTANCE
Single Stage
Two Stage
5
10
15
FREQUENCY (cm⁻¹)

Fig. 7

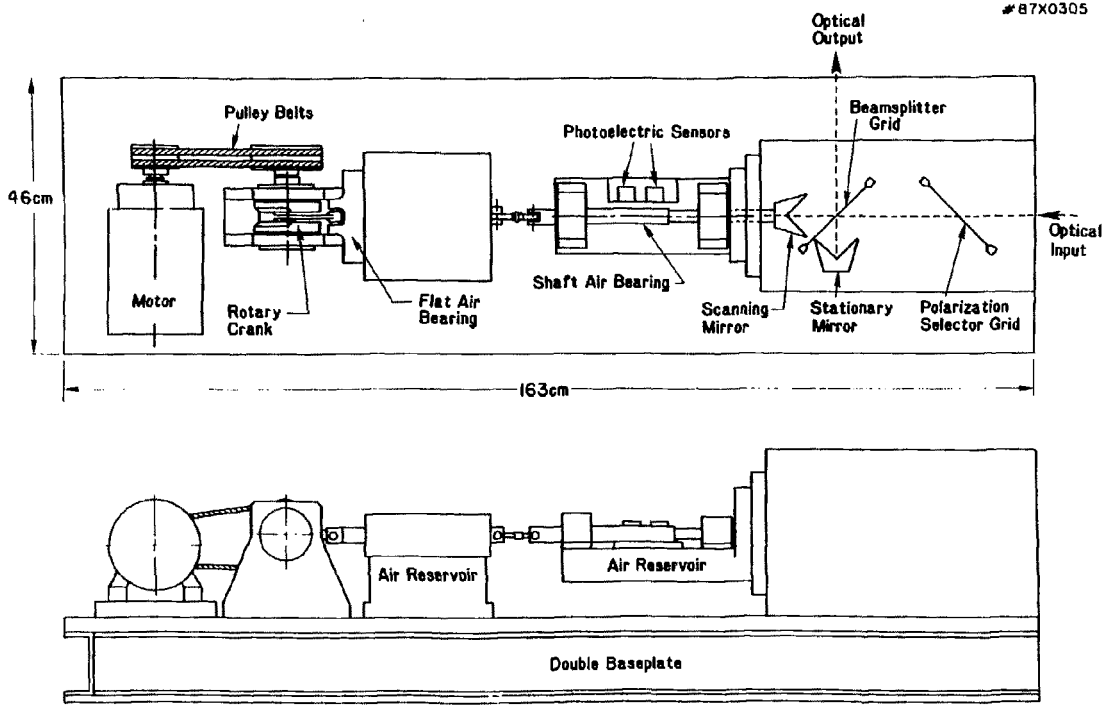
Optical Output
Pulley Belts
Photoelectric Sensors
Beamsplitter Grid
46cm
Motor
Rotary Crank
Flat Air Bearing
Shaft Air Bearing
Scanning Mirror
Stationary Mirror
Polarization Selector Grid
Optical Input
163cm
Air Reservoir
Air Reservoir
Double Baseplate

Fig. 8

#87X0303

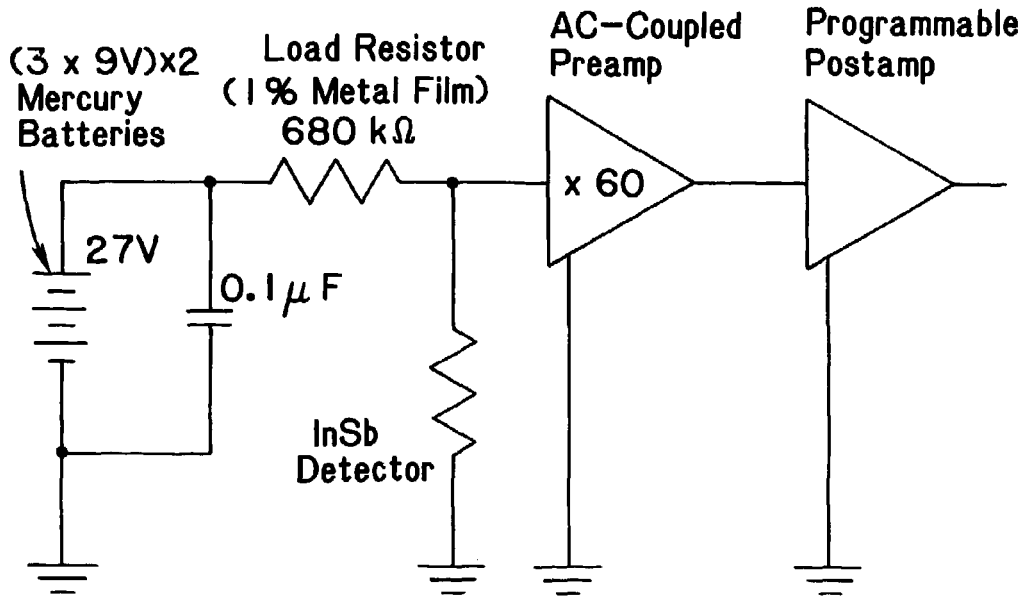

Fig. 9

#87X0293

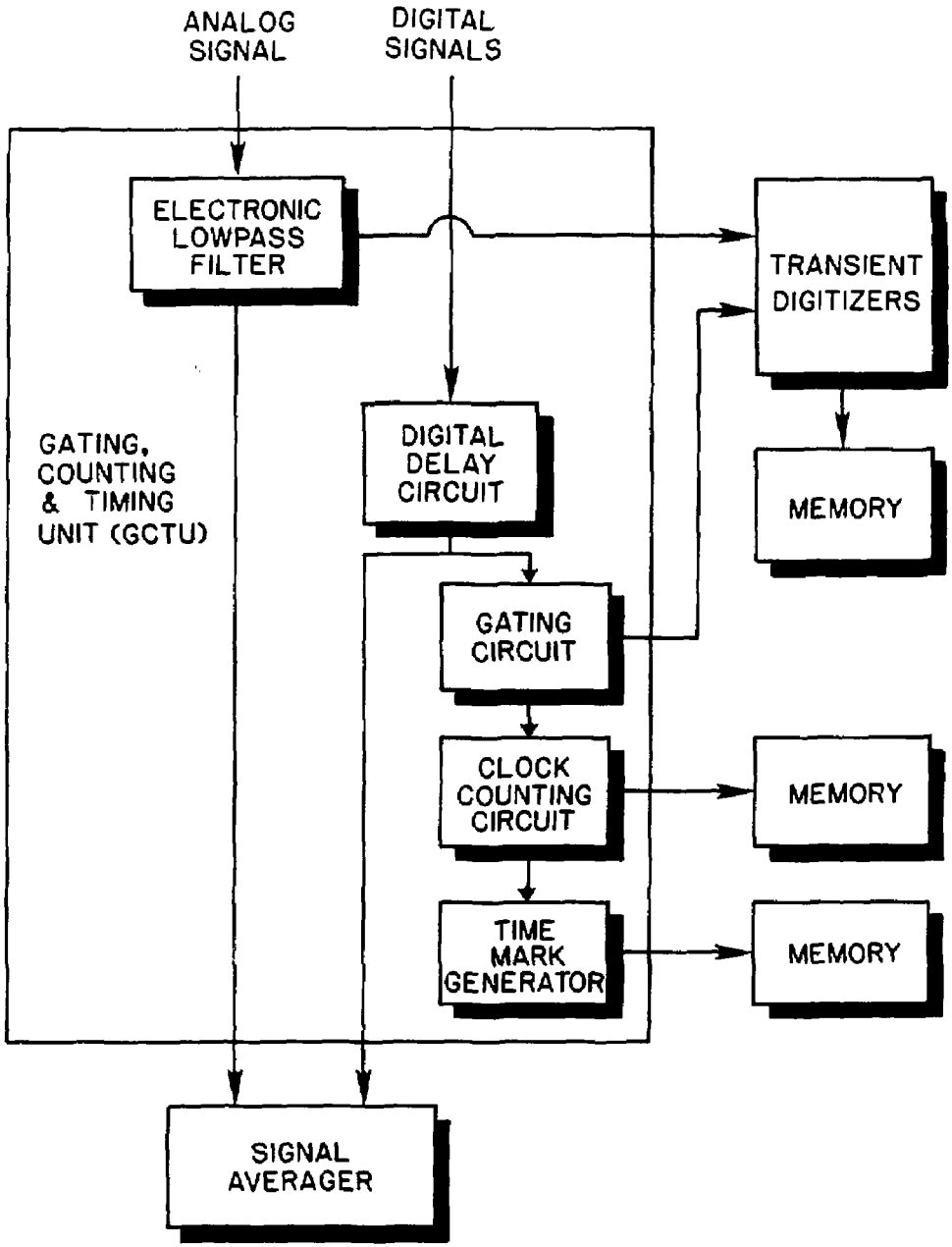

Fig. 10

#87X0292

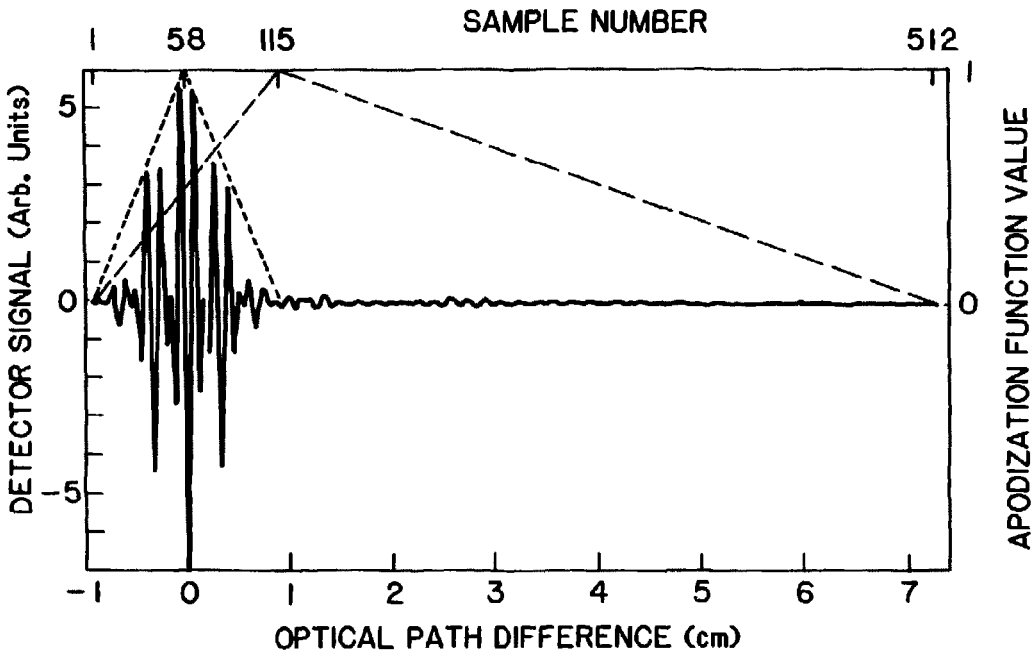

Fig. 11

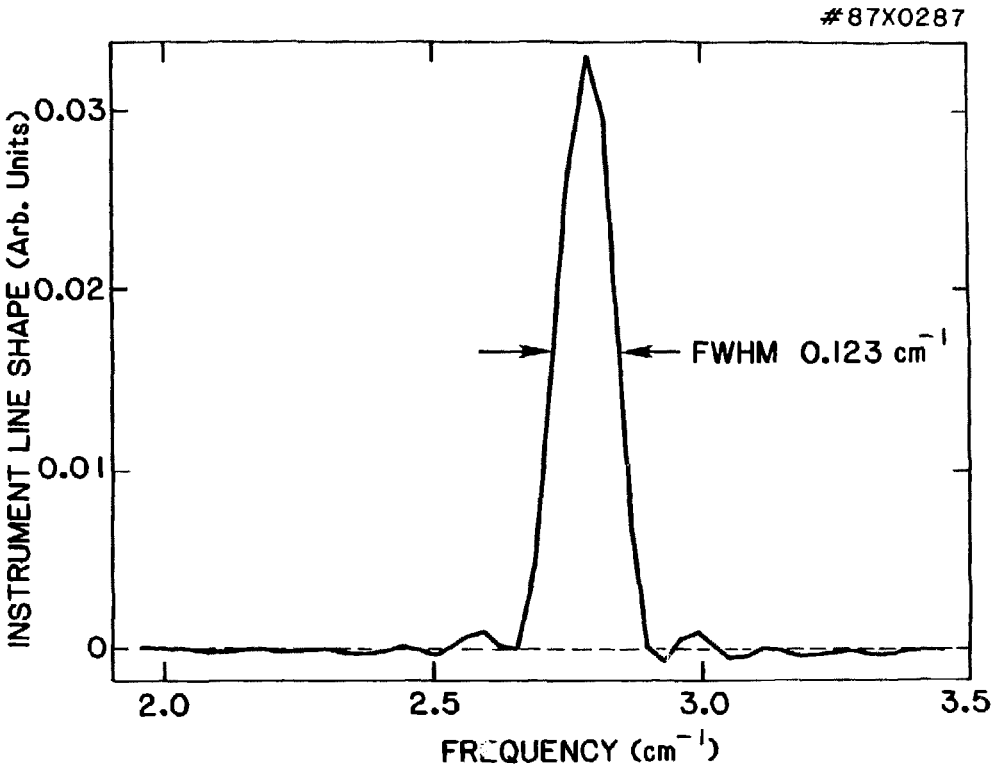
#87X0287
INSTRUMENT LINE SHAPE (Arb. Units)
0.03
0.02
0.01
0
FWHM 0.123 cm⁻¹
2.0
2.5
3.0
3.5
FREQUENCY (cm⁻¹)

Fig. 12

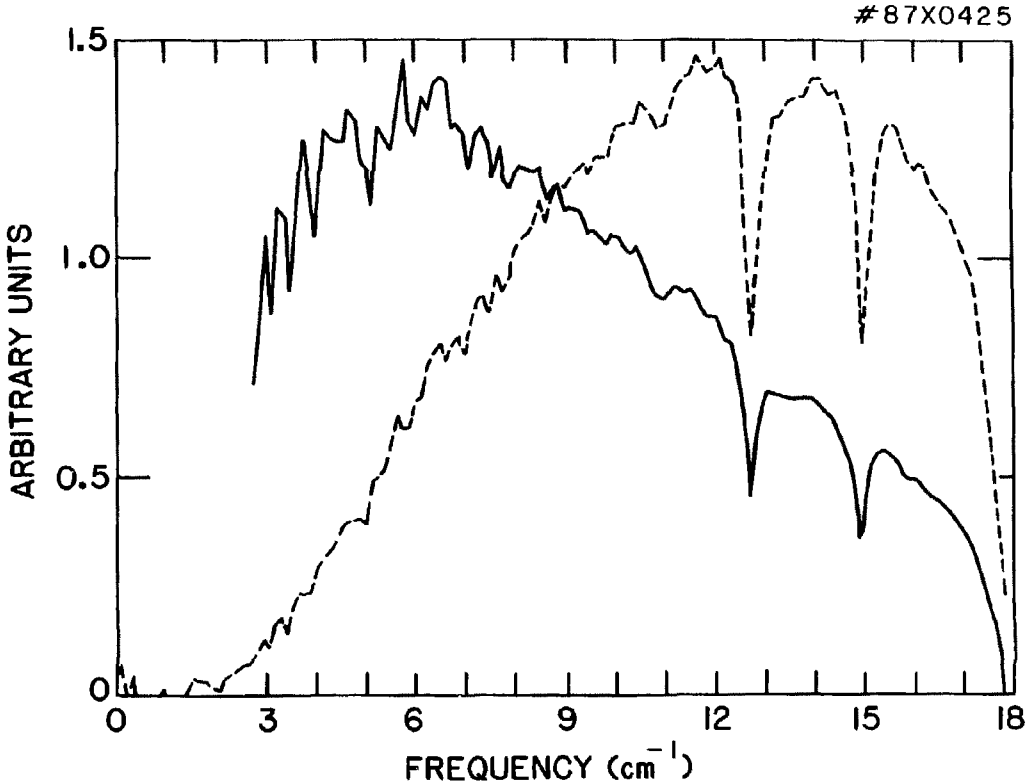
#87X0425
1.5
1.0
0.5
0
ARBITRARY UNITS
0
3
6
9
12
15
18
FREQUENCY (cm⁻¹)

Fig. 13

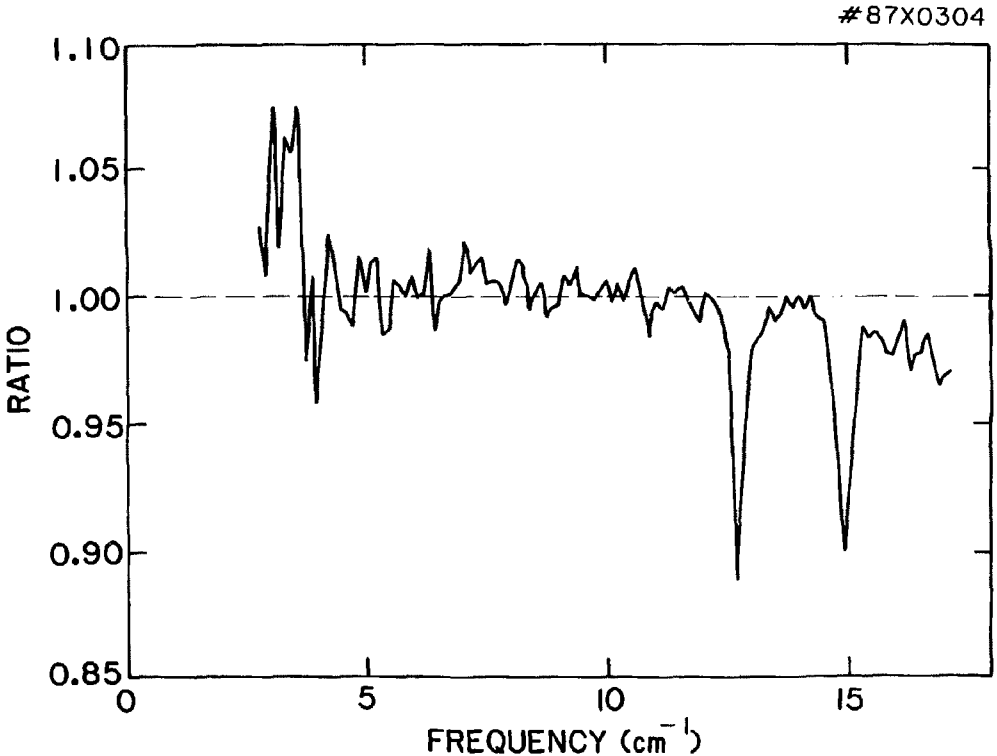

Fig. 14

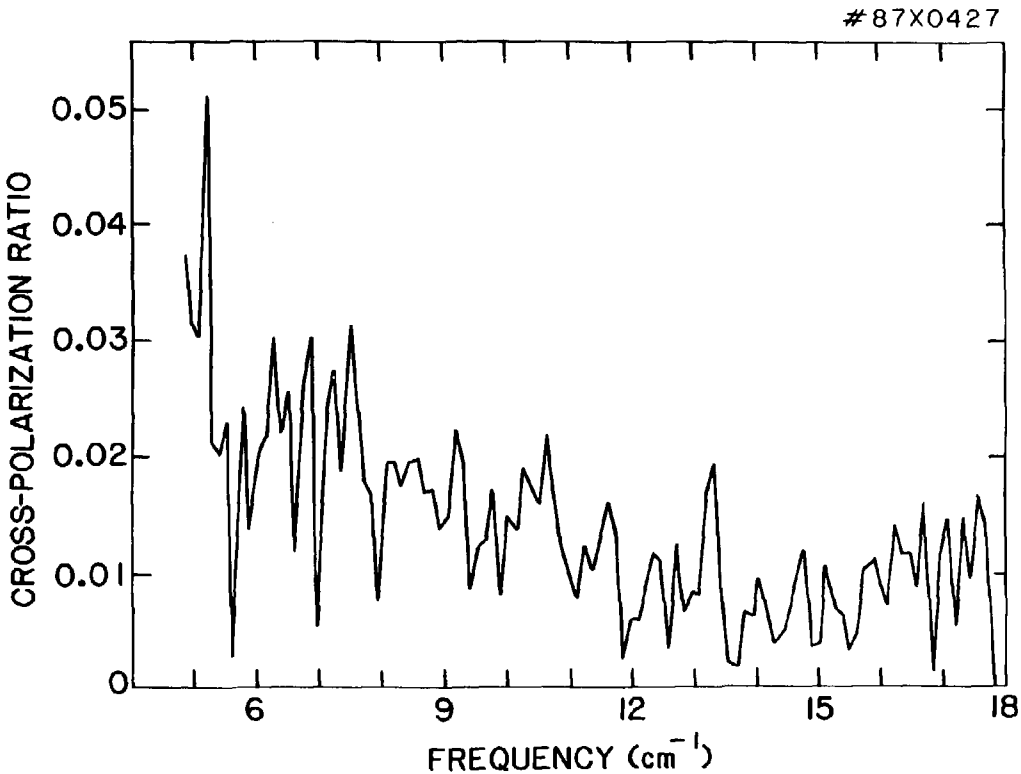
#87X0427
CROSS-POLARIZATION RATIO
0.05
0.04
0.03
0.02
0.01
0
6
9
12
15
18
FREQUENCY (cm⁻¹)

Fig. 15

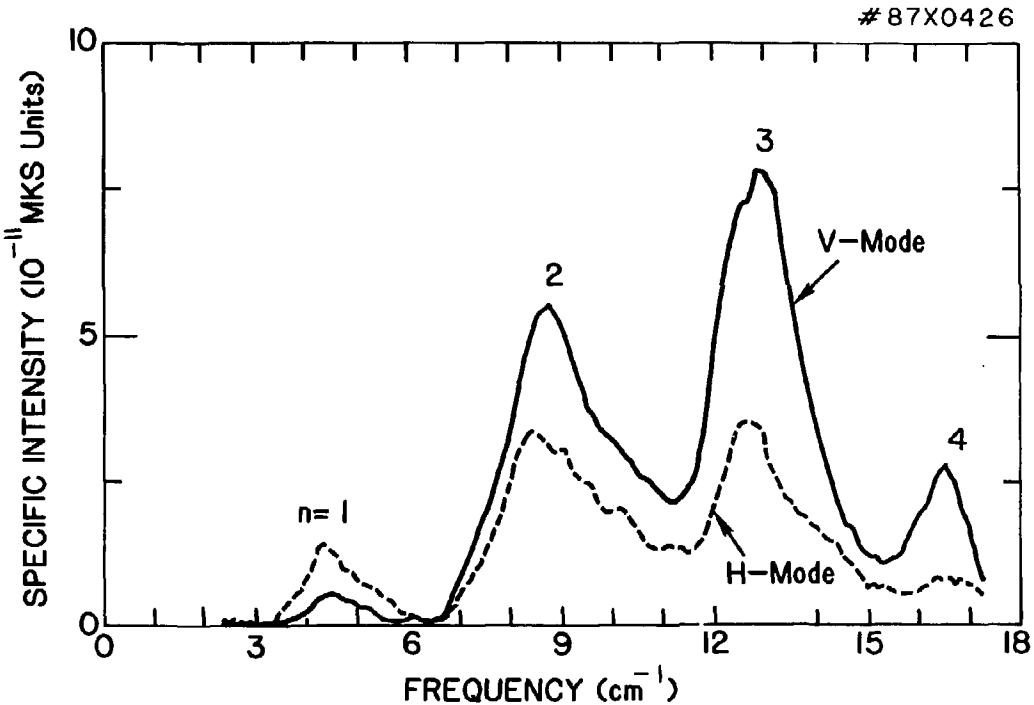
#87X0426
SPECIFIC INTENSITY (10^{-11} MKS Units)
FREQUENCY (cm^{-1})
n= 1
2
3
4
V-Mode
H-Mode
0
5
10
0
3
6
9
12
15
18

Fig. 16

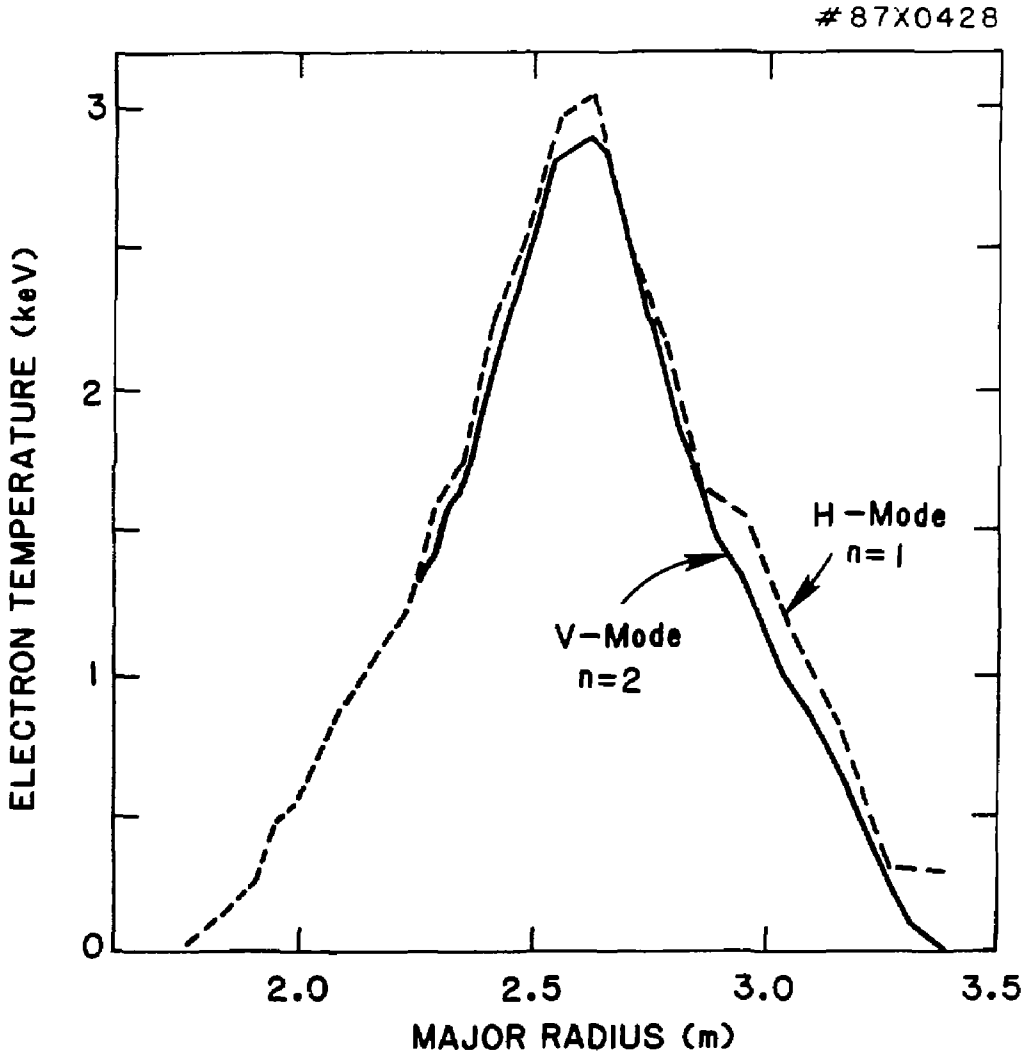
#87X0428
ELECTRON TEMPERATURE (keV)
0
1
2
3
2.0
2.5
3.0
3.5
MAJOR RADIUS (m)
H-Mode
n=1
V-Mode
n=2

Fig. 17

EXTERNAL DISTRIBUTION IN ADDITION TO UC-20

Dr. Frank J. Paoloni, Univ of Wollongong, AUSTRALIA
Prof. M.H. Brennan, Univ Sydney, AUSTRALIA
Plasma Research Lab., Australian Nat. Univ., AUSTRALIA
Prof. I.R. Jones, Flinders Univ., AUSTRALIA
Prof. F. Cap, Inst Theo Phys, AUSTRIA
Prof. H. Heindler, Institut fur Theoretische Physik, AUSTRIA
M. Goossens, Astronomisch Instituut, BELGIUM
Ecole Royale Militaire, Lab de Phys Plasmas, BELGIUM
Commission-European, Dg-XII Fusion Prog, BELGIUM
Prof. R. Boucique, Laboratorium voor Natuurkunde, BELGIUM
Dr. P.H. Sakanaka, Instituto Fisica, BRAZIL
Instituto De Pesquisas Espaciais-INPE, BRAZIL
Documents Office, Atomic Energy of Canada Limited, CANADA
Dr. M.P. Bachynski, MPB Technologies, Inc., CANADA
Dr. H.M. Skarsgard, University of Saskatchewan, CANADA
Dr. H. Barnard, University of British Columbia, CANADA
Prof. J. Teichmann, Univ. of Montreal, CANADA
Prof. S.R. Sreenivasan, University of Calgary, CANADA
Prof. Tudor W. Johnston, INRS-Energie, CANADA
Dr. C.R. James, Univ. of Alberta, CANADA
Dr. Peter Lukac, Komenskeho Univ, CZECHOSLOVAKIA
The Librarian, Culham Laboratory, ENGLAND
The Librarian, Rutherford Appleton Laboratory, ENGLAND
Mrs. S.A. Hutchinson, JET Library, ENGLAND
C. Mouttet, Lab. de Physique des Milieux Ionises, FRANCE
J. Radet, CEN/CADARACHE - Bat 506, FRANCE
Univ. of Ioannina, Library of Physics Dept. GREECE
Dr. Tom Mual, Academy Bibliographic Ser., HONG KONG
Preprint Library, Hungarian Academy of Sciences, HUNGARY
Dr. B. Dasgupta, Saha Inst of Nucl. Phys., INDIA
Dr. P. Kaw, Institute for Plasma Research, INDIA
Dr. Philip Rosenau, Israel Inst. Tech, ISRAEL
Librarian, Int'l Ctr Theo Phys, ITALY
Prof. G. Rostagni, Univ Di Padova, ITALY
Miss Clelia De Palo, Assoc EURATOM-ENEA, ITALY
Biblioteca, Instituto di Fisica del Plasma, ITALY
Dr. H. Yamato, Toshiba Res & Dev, JAPAN
Prof. I. Kawakami, Atomic Energy Res. Institute, JAPAN
Prof. Kyoji Nishikawa, Univ of Hiroshima, JAPAN
Direc. Dept. Large Tokamak Res. JAERI, JAPAN
Prof. Satoshi Itoh, Kyushu University, JAPAN
Research Info Center, Nagoya University, JAPAN
Prof. S. Tanaka, Kyoto University, JAPAN
Library, Kyoto University, JAPAN
Prof. Nobuyuki Inoue, University of Tokyo, JAPAN
S. Mori, JAERI, JAPAN
Librarian, Korea Advanced Energy Res. Institute, KOREA
Prof. D.I. Choi, Adv. Inst Sci & Tech, KOREA
Prof. B.S. Liley, University of Waikato, NEW ZEALAND
Institute of Plasma Physics, PEOPLE'S REPUBLIC OF CHINA
Librarian, Institute of Phys., PEOPLE'S REPUBLIC OF CHINA
Library, Tsing Hua University, PEOPLE'S REPUBLIC OF CHINA
Z. Li, Southwest Inst. Physics, PEOPLE'S REPUBLIC OF CHINA
Prof. J.A.C. Cabral, Inst Superior Tecnico, PORTUGAL
Dr. Octavian Petrus, AL I CUZA University, ROMANIA
Dr. Johan de Villiers, Fusion Studies, AEC, SO AFRICA
Prof. M.A. Hellberg, University of Natal, SO AFRICA
C.I.E.M.A.T., Fusion Div. Library, SPAIN
Dr. Lennart Stenflo, University of UMEA, SWEDEN
Library, Royal Inst Tech, SWEDEN
Prof. Hans Wilhelmson, Chalmers Univ Tech, SWEDEN
Centre Phys des Plasmas, Ecole Polytech Fed, SWITZERLAND
Bibliotheek, Fom-Inst Voor Plasma-Fysica, THE NETHERLANDS
Dr. O.D. Ryutov, Siberian Acad Sci, USSR
Dr. G.A. Eliseev, Kurchatov Institute, USSR
Dr. V.A. Glukhikh, Inst Electrophysical Apparatus, USSR
Dr. V.T. Tolok, Inst. Phys. Tech. USSR
Dr. L.M. Kovrizhnykh, Institute Gen. Physics, USSR
Nuclear Res. Establishment, Julich Ltd., W. GERMANY
Bibliothek, Inst. Fur Plasmaforschung, W. GERMANY
Dr. K. Schindler, Ruhr Universitat Bochum, W. GERMANY
ASDEX Reading Rm, IPP/Max-Planck-Institut fur Plasmaphysik, W. GERMANY
Librarian, Max-Planck Institut, W. GERMANY
Prof. R.K. Janev, Inst Phys, YUGOSLAVIA